

Hari P. N. Nagarajan,¹ Suraj Panicker,² Hossein Mokhtarian,² Théo Remy-Lorit,³ Eric Coatanéa,² Romaric Prod'hon,⁴ Hesam Jafarian,² Karl R. Haapala,⁵ and Ananda Chakraborti²

Graph-Based Metamodeling for Characterizing Cold Metal Transfer Process Performance

Reference

H. P. N. Nagarajan, S. Panicker, H. Mokhtarian, T. Remy-Lorit, E. Coatanéa, R. Prod'hon, H. Jafarian, K. R. Haapala, and A. Chakraborti, "Graph-Based Metamodeling for Characterizing Cold Metal Transfer Process Performance," *Smart and Sustainable Manufacturing Systems* 3, no. 2 (2019): 169–189. <https://doi.org/10.1520/SSMS20190026>

ABSTRACT

Achieving predictable, reliable, and cost-effective operations in wire and arc additive manufacturing is a key concern during production of complex-shaped functional metallic components for demanding applications, such as those found in aerospace and automotive industries. A metamodel combining localized submodels of the different physical phenomena during welding can ensure stable material deposition. Such a metamodel would necessarily combine submodels from multiple domains, such as materials science, thermomechanical engineering, and process planning, and it would provide a holistic systems perspective of the modeled process. An approach using causal graph-based modeling and Bayesian networks is proposed to develop a metamodel for a test case using wire and arc additive manufacturing with cold metal transfer. The developed modeling approach is used to characterize the effect of manufacturing variables on product dimensional quality in the form of a causal graph. A quantitative simulation using Bayesian networks is applied to the causal graph to enable process parameter tuning. The Bayesian network inference mechanism predicts the effects of the parameters on results, whereas, conversely, with known targets, it can predict the required parameter values. Validation of the developed Bayesian network model is performed using experimental tests.

Keywords

predictive modeling, metamodeling, Bayesian network, decision-making, wire arc additive manufacturing, cold metal transfer

Manuscript received August 2, 2019; accepted for publication October 18, 2019; published online November 14, 2019.

¹ Department of Automation Technology and Mechanical Engineering, Tampere University, P.O. Box 589, Tampere 33101, Finland (Corresponding author), e-mail: hari.nagarajan@tuni.fi, <https://orcid.org/0000-0002-9967-2549>

² Department of Automation Technology and Mechanical Engineering, Tampere University, P.O. Box 589, Tampere 33101, Finland

³ Sciences et Génie Des Matériaux, Institut National des Sciences Appliquées de Rennes, 20 Avenue des Buttes de Coesmes, Rennes 35700, France

⁴ Société Travaux Électriques Industrie Métropolitaine, Société par Actions Simplifiée, 12 Rue de la Gare, Chèvremont 90340, France

⁵ School of Mechanical, Industrial, and Manufacturing Engineering, Oregon State University, 204 Rogers Hall, Corvallis, Oregon 97331, USA

Nomenclature

A	= wire cross-sectional area (mm^2)
a	= parabola parameter
ALC	= arc length correction
A_p	= bead area (mm^2)
A_w	= wall cross-sectional area (mm^2)
c	= parabola parameter
CR	= cooling rate (J/s)
DC	= dynamic correction
d_m	= melt pool depth (mm)
h	= bead height (mm)
I	= current (A)
I_{end}	= ending current (A)
I_{ign}	= ignition current (A)
k	= process efficiency (%)
n	= number of layers
P_c	= capillary pressure (Pa)
P_h	= hydrostatic pressure (Pa)
Q	= heat input (J)
$SGFR$	= shielding gas flow rate (L/min)
T_b	= bead temperature (K)
t_{ign}	= ignition time (ms)
TS	= travel speed (mm/s)
t_w	= waiting time (s)
T_w	= temperature of the previously printed layer (K)
U	= voltage (V)
V	= deposited part volume (mm^3)
w	= bead/wall width (mm)
λ	= ratio between wire feed rate and travel speed
Φ	= torch angle ($^\circ$)

Introduction

The last three decades have seen additive manufacturing progress from a technique for rapid prototyping to a full-fledged manufacturing technology applied in various industries, including automotive, aerospace, medical equipment, and customized consumer products. Industry and academic research communities have identified characteristics explicitly benefited by additive manufacturing, e.g., production of mass-customized products on demand, freedom of design, high material use efficiencies, and simplified supply chains.¹ The flexibility offered by additive manufacturing processes allows manufacturers to opt for more environmentally friendly optimized product designs that eliminate waste and exhibit extended product life enabled through repair, remanufacture, and refurbishment.² The additive manufacturing technologies most commonly in use are stereolithography, selective laser sintering, directed energy deposition (DED), binder jetting, powder bed fusion (PBF), vat polymerization, sheet lamination, material extrusion, and material jetting.³ The research herein focuses on one additive manufacturing technology, namely DED using wire arc additive manufacturing (WAAM).

WAAM has gained importance because of its ability to economically fabricate metal products, including those made of aluminum, titanium, and nickel alloys.⁴ WAAM is a DED process classified by ASTM⁵ that utilizes an electric arc to melt and deposit metal filler wire. WAAM processes have high energy efficiency ($\sim 90\%$) and

high material deposition efficiency; almost 100 % of the filler material wire is deposited, resulting in reduced waste and emissions. Furthermore, the process is characterized by a high material deposition rate (up to 2,500 cm³/h) and low equipment cost, making it one of the fastest and most economical metal manufacturing processes.⁶ However, the current capability of WAAM to produce functional metal components is limited because of the relatively low accuracy and quality of the prints. The high heat input (Q) and high material deposition rate of the process induces residual stresses because of the nonuniform expansion and contraction of the material as well as the layer-by-layer deposition. These thermally induced stresses produce distortions in the part that affects part accuracy and part surface quality.^{4,6,7} In an effort to improve weld quality by reducing the high Q in WAAM, the cold metal transfer (CMT) process was introduced by Fronius.⁸

The CMT process uses high-speed digital control to alter the arc length and the thermal input during welding by mechanically feeding and retracting the wire electrode based on the duration of short circuiting, thereby controlling material transfer to the melt pool.⁹ CMT makes it possible to weld certain metals and alloys, such as aluminum, titanium, nickel, steel, and bimetal alloys, which otherwise are difficult using traditional welding processes. The major advantages of CMT are the ability to weld thin-walled structures (a few millimeters in thickness) with accuracy, reduced spatter during welding, low part distortion, improved weld bead characteristics, and higher welding speeds.¹⁰ For the same amount of material deposited, CMT requires less current compared to pulsed metal inert gas welding and generates less Q to the workpiece.

Thermal deformation that is due to accumulated heat energy and unstable weld pool dynamics because of poor parameter settings results in defects in parts manufactured using WAAM.⁶ The defects are material specific; for instance, titanium alloys are prone to oxidation, aluminum alloys develop porosity, and severe deformations and surface roughness are common in steel alloys, whereas cracks are common in bimetal alloys. Inherent residual stresses in WAAM result in part distortion, loss of geometric tolerance, delamination, and deterioration of fatigue performance and fracture resistance of the part.⁶ The selection of process parameters, e.g., welding current, welding voltage, wire feed rate (WFR), shielding gas flow rate ($SGFR$), and ambient temperature, gives rise to some of the residual stresses. Thus, modeling the interrelationships between welding parameters, part mechanical properties, and part dimensional accuracy is essential for meeting the demanding product requirements of industry. It is also an efficient manner to reduce the variability induced by the complexity of the process. In this article, the interrelationships between process parameters and final weld properties are modeled in the form of causal graphs.

Background

WAAM has revolutionized the metal printing industry with its high material deposition rates and printing speed. However, in conventional arc welding, high deposition rates are often associated with very high Q , unstable arc, and spatter. In WAAM using CMT process technology, on/off arcing is carried out in three phases, namely, the boost, burn, and short-circuit phases, in order to reduce the overall Q to the weld.¹¹ The arc is on during the boost and burn phases of the welding cycle, whereas no current is maintained during the short-circuit phase for metal transfer using the controlled dip transfer mechanism. In CMT, metal transfer is carried out by dipping the molten droplet into the weld melt pool and retracting the wire back at a specific frequency (50–130 Hz) to force the droplet to detach because of surface tension. The fast retraction movement ensures spatter-free welding because no metal transfer occurs in the gap between the wire and base material.¹² In addition, the Q to the weld only occurs during the arcing period and detachment of droplets occurs when the process is current free.¹⁰ In this research, a CMT welder (Fronius CMT Advanced 4000) was used to characterize the effects of process parameters on the weld dimensional accuracy.

CMT WAAM TECHNOLOGY

The CMT welder used in this research functions as a closed system with only a small number of principal parameters available for tuning by the operator. The user employs synergic lines that have been predesigned by the CMT welder (Fronius) for combinations of different filler materials, filler wire diameters, and shielding

gases. These synergic lines help control the voltage and current cycles linearly during welding for the desired *WFRs* in each phase of the CMT process while also controlling the parameters for filler wire retraction.^{10,13} To maintain predesigned synergic lines, the user is allowed to choose the required *WFR*, which, in turn, defines the current and voltage cycles, in addition to two fine-tuning parameters: arc length correction (*ALC*) and dynamic correction (*DC*). *ALC* and *DC* influence the average power and deposition rate. In addition, *ALC* influences the bead characteristics, such as bead shape, dilution, and penetration.⁷ In the work herein, the fine-tuning parameters have been kept constant, whereas the *WFR* is varied across the experiments to characterize its effect on modeled targets, namely, width (*w*) and height (*h*) of the bead/wall.

EFFECT OF WELDING PARAMETERS DURING LAYERED MANUFACTURING

To establish process settings, the user defines the filler *WFR* and travel speed (*TS*) for industrial robot movement. The *WFR* governs the average deposition rate of the filler material (wire), the working current, and the working voltage based on the synergic line to ensure *Q* is sufficient for proper melting of deposited wire.¹³ The *TS* is defined in the Rapid code that commands the welding robot (ABB 4600 40/2.55) and influences the weld deposition rate. For the same *WFR*, higher *TS* will reduce the deposition rate. Tuning the *WFR* and *TS* can control the deposition rate and, hence, the dimensions (*w* and *h*) of the weld bead produced using WAAM. Further, the combination of *WFR* and *TS* defines the deposition rate and *Q*, and, consequently, the interpass temperature (*T_w*) of each layer before deposition. *Q* is given by equation (1) (Näkki 2018)¹³:

$$Q = \frac{P}{TS} = k \times \frac{I \times U}{TS} \quad (1)$$

where *P* is the welding power, *TS* is the travel speed, *k* is the process efficiency factor (0.85 for CMT¹⁴), *I* is average current, and *U* is the average voltage. The *WFR* and *TS*, and the resultant *Q* and *T_w*, have a high influence on the melt pool shape and grain structure of the solidified material.¹⁵ Specifically, the *T_w* plays a major role in determining the grain structure and, in turn, the mechanical properties of a part produced using WAAM. For instance, a higher *T_w* generally provides finer grain structure and improved toughness for high-strength steel. However, this trend tends to reverse as *T_w* exceeds 260°C;¹⁶ increasing the *T_w* beyond this limit causes the weld pool to puddle and collapse, affecting the geometric quality of the part. Thus, controlling the heating and cooling of the part to maintain an optimized *T_w* is essential for achieving a good quality weld.

The *Q* directly relates to the ratio between *WFR* and *TS*. This ratio plays an important role, and the experimental process has shown that relatively precise boundaries exist for its value. In order to obtain good dimensional quality in the weld, it is necessary to model the influence of this ratio and to tune the parameters not to exceed its value limits during printing. It is also important to notice that the ratio (*WFR/TS*) is dimensionless. This dimensionless ratio plays the role of a model invariant. This invariant governs heat transfer, material deposition, and, ultimately, the bead shape after solidification. This invariant can be rediscovered using dimensional analysis theory.¹⁷ The ratio can be more easily presented using the conservation of mass between the wire added and deposited geometry¹⁸ (equation (2)):

$$\frac{WFR}{TS} = \frac{CSA}{A_{wire}} \quad (2)$$

where *A_{wire}* is the wire cross-sectional area and *CSA* is the layer cross-sectional area. This dimensionless ratio is used as supplementary information in modeling the process, which aids in improving the accuracy of the model.

In the case of the wire laser additive manufacturing (WLAM) technology, Ding et al.⁴ indicated that the wire feed orientation influences droplet transfer and the quality of the deposit. Front feeding, back feeding, or side feeding are possible, and differences in quality for different metallic materials have been reported depending on feed direction. Torch angle (*Φ*) is not well documented as a factor in prior work. The possible influence of this factor is evaluated for a single-bead geometry through experiments using the WAAM process, as described

in the Methodology section. Furthermore, with WLAM technology, the deposition width is mainly determined by the laser power, whereas the height is influenced more by welding speed. The deposition area is determined using the ratio of the *WFR* to the welding speed. Increasing power for WLAM implies a decrease of the deposition height and an increase of the deposition width. These experimental results could be adopted for WAAM because CMT technology implies that the power is directly controlled by the *WFR* through the control algorithm of the predefined synergic lines from the CMT manufacturer. An increase in power implies an increase in *WFR* and should also lead to a decrease in deposition height and increase in deposition width. The hypothesis will be verified experimentally as described in the Methodology section and the Discussion and Results section of the article. The effect of process parameters studied in this section and existing models from literature can be used to develop an initial causal graph. A causal graph model can provide direction to perform knowledge-assisted experimental modeling of bead geometry.

MODELING OF SINGLE-BEAD AND MULTIBEAD WELD GEOMETRIES

Analytical models for single-bead and multibead welds have been previously developed to predict the bead shape using the geometry and temperature of the melt pool as central indicators. Prior work has followed a modeling strategy in which knowledge such as rules and theories are used to formulate models representing the multiphysical phenomena. The models are derived from theoretical analysis that focuses on subprocesses with idealized assumptions. The actual multiphysical system of WAAM technology involves numerous interactions among these subprocesses. Such complexity can be difficult to elucidate. For example, the thermal model from Rosenthal¹⁹ and its later developments by Nguyen²⁰ are often used as central references in such efforts because thermal phenomena are fundamental in understanding the weld geometry as well as the mechanical properties of the weld. Analytical modeling aims at developing predictive models relying on a solid understanding of the process physics. The approach aids in developing robust models capable of integrating the complexity of the welding process, specifically in multibead geometries. Another approach relying on more simplified models involves experimental measurements using inline thermal scanning. Kwak and Doumanidis,²¹ for example, advocated the necessity of using inline thermal scanning during welding. Complex, open-loop, multibead predictive models are inaccurate for predicting h , w , and mechanical properties because they are often attendant with high errors because of the presence of noise and uncontrollable parameters, which are often unavoidable.

Nevertheless, an understanding of the physical phenomena involved in WAAM and other welding processes is needed to characterize the complex interrelations between process parameters and modeling targets. Elements such as layer geometry, deposition speed, thermal energy absorbed per layer, successive energy inputs, and thermal conduction, convection, and radiation, are shown to have strong interactions with bead geometry and part mechanical properties. In the analytical model developed by Ríos et al.,¹⁷ the shape of the deposited melted material was analyzed using capillarity theory. The melt pool is subjected to two opposite forces (i.e., capillarity forces and hydrostatic forces). Although real weld droplets are in the form of ellipsoids, effort was made to constrain the welding conditions to obtain a melt pool cross section agreeing with the hypothesis that weld droplets are circular. This analytical approach represents the physical phenomena in welding with an extensive level of detail and allows the integration of previous analytical efforts. However, typical analytical models involve simplifying hypotheses to cope with modeling complexity.¹⁷ Such hypotheses are required in simplifying otherwise intractable mathematical calculus difficulties, which simultaneously limit the scope and generality of models produced.

The models presented in the form of causal graphs in **figures 1** and **2** summarize this modeling approach for single-bead and multibead geometries. In the specific case of modeling a single-bead geometry, different shape approximation models have been proposed, including parabola, cosine, and arc models.^{4,22} A model for overlapping beads has also been developed using this approach for parallel yet slightly overlapping beads. The authors model the overlap by determining the critical center distance between two successive weld deposits, the size of the critical valley, and the size of bead overlap area using a tangent overlap model.⁴ This model

FIG. 1

Causal graph model summarizing literature on single-bead wire additive manufacturing.^{4,22}

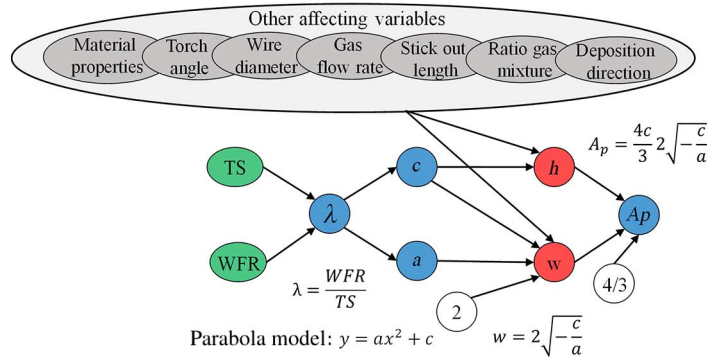
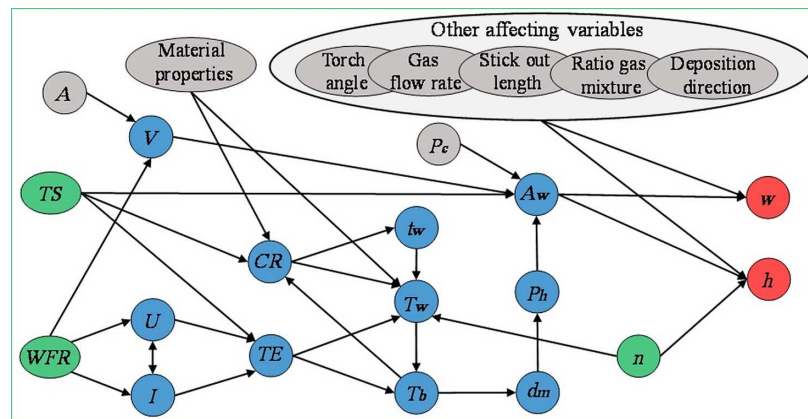


FIG. 2

Causal graph summarizing literature on multibead wire additive manufacturing.^{1,17,19-21}



does not fully meet the needs of this research to model multibead geometry, wherein beads are deposited on top of one another for layered manufacturing. Nevertheless, such modeling efforts provide useful information by helping detect important parameters that influence the bead geometry, such as layer height, wall width, effective wall width, remelting, apparent weld pool depth, droplet radius, and deposition angle. Aside from modeling strategy, we find metamodels, also known as surrogate models, which are often statistical models that represent unknown manufacturing systems. Metamodeling focuses on the input/output parametric values while ignoring the complex interrelationships within the unknown internal system. Hence, these approaches do not require detailed knowledge of the underlying physical phenomena.²³ In place of physical knowledge, the predictability of metamodels relies upon statistical features, such as sampling strategy and modeling algorithms, requiring experimental data. Metamodels can optimally reduce the inaccuracies that arise from incomplete knowledge.

Depending upon the visibility of the internal design, structure, and implementation of the computational models, they can be classified as white box, black box, and gray box models.²⁴ White box models are transparent, meaning the internal relationships between variables, physical phenomena, and outputs are known, whereas black box models are opaque in terms of knowledge about the internal relationships. Gray box models combine the attributes of both white box and black box models in the sense that these models combine a theoretical structure of the system being modeled along with data to provide a comprehensive model. For the interest of this study, the dimensional analysis conceptual modeling (DACM) framework by Coatanéa et al.²⁵ is used to synthesize white

box and black box approaches to form a gray box model. Numerical models are similar to white box models and are often developed for modeling simple subprocesses, but they imply heavy computational requirements. However, numerical models can be used as a way to run “virtual experiments.” If properly calibrated, they can improve the predictability of a black box component of a metamodel.

Next, the background study on modeling welding bead geometry is translated into an initial graph-based model using the DACM framework, which is then verified using empirical modeling in the Methodology section of this article.

DACM

The DACM approach has been employed in this research to analyze and summarize the results of different models that currently exist in literature for WAAM. This approach uses causal graphs to represent cause-effect relationships in complex systems.²⁵ The method is different from flowcharts, functional, or integrated computer-aided manufacturing definition for function modeling (IDEF) representations²⁶ in the sense that its purpose is to present the set of cause-effect relationships that are domain-dependent and not the control logic of a system. In this research, the effect of input parameters on two desired outputs, the height and width of a vertically printed wall, are studied. The causal relations can be extracted from a set of known equations or from other techniques, such as dimensional analysis or organs modeling, derived from a combination of bond graph theory, organs modeling, and functional modeling approaches.^{25,27}

The selection of the articles presented in the current effort to model the WAAM process was completed using three key criteria. First, the research should support the creation of a simple model for geometry modeling and mechanical property modeling of WAAM produced parts. Second, the process reported by the research should exhibit globally similar deposition and thermal phenomena as for the WAAM process. Third, the modeled phenomena should be compatible with the modeling of the CMT WAAM used in this research.

For causal modeling, some of the analytical tools from DACM are used in the research reported herein. The causal graphs shown in **figures 1** and **2** summarize the literature review. The graphs are color coded to represent different variables and targets as nodes. A node is a variable of the model and can take on one of four colors. Independent variables are represented in green and can be changed to modify the objectives of the model. Independent variables cannot be directly modified by other variables of the model. Usually these variables have to be selected in priority to pilot and control model outputs. Dependent variables are represented in blue and can be controlled indirectly via the variables affecting them. Consequently, dependent variables are usually not the first choices to control a complex process. Exogenous variables are represented in gray and are usually imposed by the external environment or by technical requirements. In our context, exogenous variables are also variables fixed by other literature models. Often, improvements in model accuracy can be obtained by converting gray (exogenous) variables into green (independent) controllable variables, which should be specifically done if the variables are known to have a high influence on the process. Finally, objective, or target, variables are represented in red and are usually a specific type of dependent variables. Targets have specific importance in a system because they represent the outcomes of a process. The DACM causal graph shows the flow of the modeled process from its independent (controlling) variables to its dependent objective/target variables. This representation is of interest in the context of this research to provide an initial direction in the modeling of bead geometry. **Figures 1** and **2** show the causal relationships for single-bead and multibead models, respectively. As discussed previously, two independent variables, *WFR* and *TS*, are used to model the bead geometry. For the multibead geometry, one additional variable, the number of layers (*n*), is added to the initial set of independent variables.

The articles reviewed consider those parameters as fixed constants and, hence, they are represented as exogenous variables. The same choices have been made in the current article by the authors. Nevertheless, it should be noted that exogenous variables could be considered as independent variables in future modeling efforts by incorporating additional phenomenological process knowledge.

From the causal graphs, it can be seen that two variables are required in the WAAM process to generate a model of the wall width and three independent variables are needed for modeling wall height. The graphs provide multiple paths from the independent variables (i.e., WFR , TS , and n) to the two variables of interest here (i.e., w and h). In future research, several parameters considered as exogenous variables here will be integrated into the set of independent variables. This modification allows for expansion of the scope of the causal models while consequently integrating additional parameters that jointly affect bead geometry and mechanical properties. A closer look at some other features of the graphs previously depicted shows that for the single-bead model, a dimensionless ratio between WFR and TS is used to model the bead geometry.

The dimensionless ratio exhibits several interesting properties of dimensionless numbers. Dimensionless variables are used extensively in fluid dynamics to represent complex and multidimensional phenomena.¹⁸ They reduce the dimensionality of a complex problem by integrating multiple intricate phenomena into one or more dimensionless groups of variables. Also of interest is that the mathematical expressions of dimensionless numbers take the form of power laws representing nonlinear phenomena, such that $A = y \cdot x^n \cdot z^m$, where A is the dimensionless group, y is an output variable of the phenomena, and x and z are independent or dependent variables influencing the phenomena. In the DACM method, all phenomena are represented using power laws and summations or subtractions. This will be evident in the later part of the article during the development of the prediction models.

The background study and initial causal graphs were used to develop an experimental approach to model bead width and height as next explained in the Methodology section.

Methodology

The Background section analyzed the current literature models and concluded that the bead geometry in WAAM can be modeled using a small number of independent variables. This conclusion was experimentally verified for a single-bead geometry as explained in what follows. Two experimental efforts have been carried out in this research. The first focuses on single-bead geometry by varying nine independent parameters using a Taguchi design of experiment (DOE) approach. The second effort focuses on building straight walls with stacked beads (varying the n) and constant length (80 mm). A rectangular plate (300 by 200 by 20 mm) made of mild steel was used as the base plate for depositing the single-bead and multibead geometry. The base plate was cleaned with ethanol before the first print and brushed using a wire brush before each subsequent print job. For multibead printing, the first layer was printed onto the base plate using a TS of 10 mm/s and a WFR of 6 m/min—settings that were held constant for printing the first layer for all the experiments and validation prints. A higher WFR was chosen for the first layer to avoid incomplete deposition of the subsequent layers. A higher WFR provides a thicker base layer and additionally preheats the base plate, which results in better bonding between consequent layers. **Table 1** reports the experimental welding parameters, consumables, and equipment used.

EXPERIMENTAL APPROACH FOR MODELING SINGLE-BEAD GEOMETRY IN CMT

The nine input parameters that were considered for the study are ignition time (t_{ign}) (ms), ignition current (I_{ign}) (A), ALC (%), WFR (m/min), TS (m/min), $SGFR$ (l/min), Φ (°), ending time (T_{end}) (ms), and ending current (I_{end}) (A). Three levels were chosen for Φ , whereas four levels were chosen for the eight other input parameters. It was observed that printing with the Φ set at 110° had high weld deposition rate, resulting in increased width of the part. In addition, the impact of I_{ign} and I_{end} on the shape of the bead was observed during experiments. It was seen that a lower I_{ign} (90–120 A) is required to maintain uniform bead structure. The I_{end} had to be set in a higher range (125–155 A) to maintain a level bead across the length of the wall. A mixed-level orthogonal plan was used for the DOEs. An L32 orthogonal design comprised of 32 experiments was chosen for each Φ , resulting in a total of 96 experiments. The procedure was repeated once to ensure repeatability. Based on the number of variables and their chosen levels, the total number of experiments to test all the combinations between variables would

TABLE 1

Weld parameter settings, consumables, and equipment for single-bead and multibead geometries

Equipment/Material/Method	Single Bead	Multi-Bead
Base plate size (material)	300*200*20 mm (mild steel)	300*200*20 mm (mild steel)
Bead length (material)	50 mm (TD MAK-10S)	80 mm (TD MAK-10S)
Robot	ABB 4600 40/2.55	ABB 4600 40/2.55
Shielding gas type	MISON 8 (Ar + 8 % CO ₂ + 0.03 % NO)	MISON 8 (Ar + 8 % CO ₂ + 0.03 % NO)
DOE type (number of experiments)	Taguchi L32 (96)	Full factorial (27)
Measurement of outputs	Laser scanning	CMM, profilometer
Parameter of Study (levels)		
Ignition time (t_{ign})	(100, 200, 300, 400) ms	F (400) ms
Ignition current (I_{ign})	(90, 100, 110, 120) A	F (46, 47.7, 49.2) A
Arc length correction (ALC)	(-15, -10, 0, 15) %	F (0) %
Wire feed rate (WFR)	(53.3, 58.3, 63.3, 68.3) mm/s	(33.3, 41.6, 50) mm/s
Travel speed (TS)	(6.6, 8.3, 10, 11.6) mm/s	(10, 11, 12) mm/s
Shielding gas flow rate (SGFR)	(14, 16, 18, 29) L/min	F (14) L/min
Torch angle (Φ)	(70, 90, 120) degrees	F (90) degrees
Ending time (T_{end})	(100, 200, 300, 400) ms	F (400) ms
Ending current (I_{end})	(125, 135, 145, 155) A	F (46, 47.7, 49.2) A
Number of layer (n)	F (1) layer	(9, 12, 15) layers
Wire stick out	F (15) mm	F (15) mm
Interpass temperature	N/A	150 °C

Note: ABB = ASEA Brown Boveri; CMM = coordinate-measuring machine; F = fixed parameter; N/A = not applicable.

be $N_{tot} = 3^1 * 4^8 = 196,608$ experiments. Thus, the current experiments conducted represent only 0.04 % of a full-factorial combination of the nine factors.

The printed beads were scanned using a laser scanner (Romer Absolute Arm Laser Scanner) set to the fine resolution mode, which generates point clouds for features as small as $\sim 20 \mu\text{m}$. The point clouds generated were used to create a three-dimensional (3-D) surface using Polyworks 3-D metrology software.

The created surfaces were used to measure and record data about the h and w of the bead along its length. Cross sections were created along the length of the bead on the 3-D surface model, separated by a distance of 1 mm. The h and w of the bead were measured at each of these cross sections, averaging 560 measurements per bead. These data points were then used to generate plots showing the variations in height and width along the length of the bead. The deviations in w and h are indicators of the quality of the weld bead and its relation to the variations in the different input parameters.

In the second experimental effort, only three input variables were considered to model w , namely, the WFR, the TS of the robot, and the n . WFR and TS were seen to have the greatest influence on the outputs, w , and h for the single-bead geometry. Thus, these two parameters were varied for the multibead geometry. To account for the buildup of h that is due to successive printing of layers, the n was also considered for the experiments. These choices are explained further in the Discussion and Results section. Intermediate variables, such as T_w and Q , are considered in the DOE for obtaining a good quality weld. Variables such as ALC and DC are omitted in this study. Exogenous variables, such as SGFR, shielding gas mixture percentage, and wire stick out length, were also omitted from the model as indicated in the Background section and explained in the Discussion and Results section. Focusing on a few independent parameters offers significant modeling value because it enables generation of simple but precise models. The approach selected can also be seen as metamodeling. This metamodeling strategy does not provide a description of all the details of the process but rather focuses on the central parameters initiating the complex WAAM process results. The assumptions and observations from the first experimental effort have been applied to the second experimental effort to model multibead weld geometry as explained next.

EXPERIMENTAL APPROACH FOR MODELING MULTIBEAD GEOMETRY IN CMT

The experimental setup has been described at the beginning of the Methodology section, and **Table 1** lists the chosen process parameter values, consumables, and equipment used in the study. The preliminary analysis conducted on the outputs of the first set of experiments for the single-bead geometry and the background study led to the identification of welding parameters that have higher impact on the quality of weld deposition. A DOE approach using a full-factorial design was used to model the influence of key process parameters. A full-factorial DOE explored all the possible combinations of factors and levels.²⁸ Following the observations from the previous experiments for single-bead geometries, the full-factorial DOE was developed for 27 print jobs with 3 levels for *WFR*, *TS*, and *n* (**Table 1**). A full-factorial DOE (Appendix A) was feasible for the multibead geometry because of the low number of input parameters chosen for this study. However, for a more extensive DOE with more factors and levels, it becomes challenging to perform a full-factorial DOE. In such a case, a Bayesian approach to DOE is recommended.²⁹ The Bayesian experimental design framework allows the user to conduct the minimum number of experiments required to characterize a process with a certain level of precision while proposing stopping criteria.

Previous experiments found that *WFR*, *TS*, *Q*, and T_w are the most influential parameters in CMT WAAM. As seen in the Background section, *Q* is dependent on *WFR* and *TS*. The T_w is affected by the *Q* as well as the waiting time between layers. To obtain a good weld, it is necessary to maintain good control of the *Q* and resultant T_w to ensure continuous deposition of the weld and to avoid spatter and microexplosions in the melt pool because of high *Q*. From experiments, a *WFR* value above 4 m/min resulted in excessive heat buildup in the part for layer number 7 for mild steel. For the DOE, the *WFR* value was kept below 4 m/min. Further, experiments showed a dimensionless *WFR* to *TS* ratio (λ) under 2.5 led to poor quality parts, mainly because of a low deposition rate (**fig. 3A**). The upper limit for the λ ratio was found to be five. In future research, the ratio will be used to calibrate our Bayesian model, which is presented in what follows, to dynamically correct predicted parameters. The ratio will be used as a constraint for the model (**fig. 4**).

In addition to *WFR* and λ ratio limits, it was found that a T_w between 100°C to 200°C yielded the best quality welds (**fig. 3B**) for mild steel. From the first experimental approach and resulting parts (**fig. 3**), it can be observed that warpage is more pronounced at the start of the weld because of the heat sink effect of the base plate and is less evident at the end of the weld bead because of the flowing of molten metal.³⁰ The resultant layer height at the start of the bead is higher than the rest of the bead. In the Fronius CMT process, the *WFR* determines the welding current and, in turn, the *Q*. Thus, the I_{ign} and I_{end} were tuned during printing as a percentage of working current.

FIG. 3 (A) DOE combinations that resulted in incomplete deposition; (B) profile of a printed multibead geometry for T_w between 100°C and 200°C; (C) back and forth printing pattern followed by the robot to generate the multibead geometry.

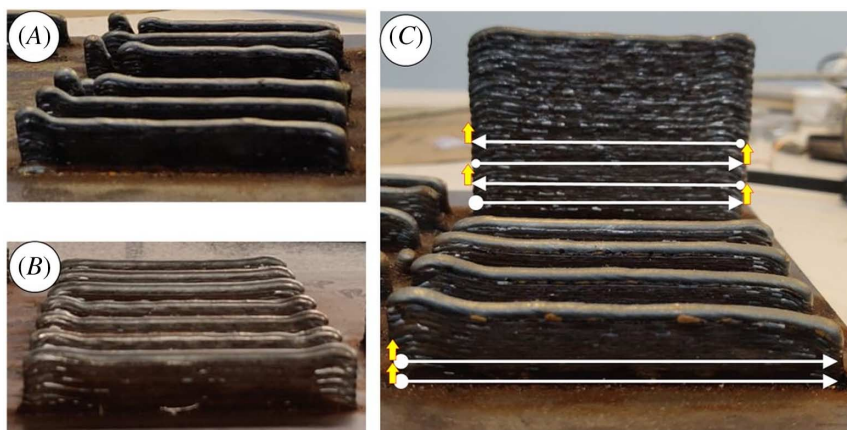
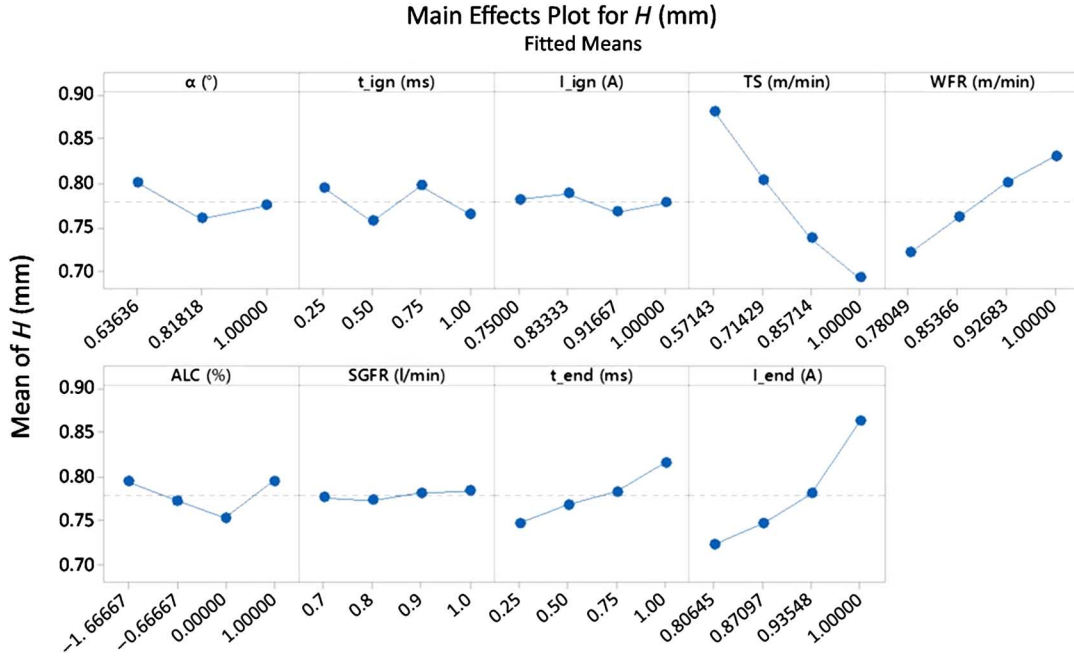


FIG. 4 Effect of input variables on the mean height for a single-bead geometry.



These values were tuned to match the lowest WFR value (1.2 m/min) obtainable for the filler wire chosen based on the predefined synergic line from the manufacturer and according to equation (3):

$$I_{ign} = I_{end} = \frac{1.2}{WFR} \times I_{working} \tag{3}$$

To compensate for the flowing of molten metal at the end of the welding pass, the t_{ign} and T_{end} were kept constant at 400 ms.

In addition to the I_{ign} and I_{end} , a unidirectional printing pattern was seen to create a significant drop in height at the end of the bead (fig. 3C, front-most wall). In unidirectional printing, the peak current is constantly applied at the start of the wall, resulting in higher material deposition and, consequently, reduced height at the end of the wall. Thus, a back and forth printing pattern was chosen for printing the part to avoid this issue and normalize the height of the bead throughout its length (fig. 3C, back-most wall). A thin-walled structure, shown in the figure, was selected for the DOE. During printing, the T_w was measured using a contact type digital thermal probe (i.e., Center 314 humidity temperature meter with a K-Type thermocouple). Each layer was allowed to cool until the T_w reached 150°C. The w and h of the printed walls were measured using a coordinate-measuring machine (SIP CMM5 High Precision 3-D CNC measuring machine) with a resolution of 0.1 μm . Measurements were taken along the length of each wall at five locations. It was seen that the variations of w and h were in the range of 25–280 μm and 64–260 μm , respectively. The average measured values of w and h were chosen for regression modeling. The experimental results were used to empirically model the w and h of this multibead geometry for CMT WAAM.

MODEL ASSUMPTIONS AND CONSTRAINTS

The models developed in this article are confined to a set boundary. In this respect, the variables classified in the exogenous category are located outside the borders of the studied system. This does not remove their influence on the system but rather highlights the lack of control of these parameters. Thus, parameters such as the type of

filler material, material properties, and part geometry are considered as being imposed on the engineer and cannot be modified. The material properties, such as specific heat capacity, thermal conductivity, and emissivity, influence the heating and cooling rate during printing. However, for a specific material system, the effect of material properties on the heating and cooling rate can be considered constant. In addition, the part geometry influences the printing path chosen and, consequently, the heating characteristics during welding. In CMT WAAM, the λ ratio (WFR/TS) defines the rate of heating and material deposition. The effect of material properties on the thermal properties of the part are incorporated in this ratio. In our model, a constraint related to this ratio, $\lambda = [a,b]$, as presented in [figure 1](#), is shown to control the heat deposition. For the material used in this study (mild steel), $a = 2.5$ and $b = 5$ are the limits of the λ ratio, allowing a close to constant heat deposition independent of the part geometry. Thus, the part geometry and printing path are considered as exogenous variables in this study. Similarly, the T_w is added to the current model as a constraint, such that its value is limited based on the type of filler material used. The T_w determines the rate of successive heating and cooling of the weld and influences the quality of printing. The effect of this variable is explained in detail in the Background section. Thus, a constraint, T_w less than a set value ($c = 150^\circ\text{C}$), is defined for the specific filler material used in this work.

EMPIRICAL MODELING OF WIDTH AND HEIGHT FOR A MULTIBEAD GEOMETRY IN CMT WELDING

Single-bead and multibead geometries were printed based on the devised DOE plans. The data collected from subsequent measurement of these prints were then analyzed to identify correlations between the input parameters and the outputs. Based on the first DOE, the thin-wall structures were printed using low carbon steel alloy wire (TD MAK-10S).³¹ A multivariable nonlinear regression analysis for w and h was performed to generate a curve fit for the data obtained from the experiments. A power law form was selected to adjust the curve to the experimental data. The approach selected to compute the regression equation was based on a conventional approach for resolution of a system of linear equations. The power laws were first linearized using a natural logarithm transformation, and a matrix operation was then applied using the general formula shown in the following equation:

$$[E] = [A_{ln}^T \cdot A_{ln}]^{-1} \cdot [A_{ln}]^T \cdot [B] \quad (4)$$

where $[E]$ is a vector representing the exponent of the power before multiplication by a natural exponent. Matrix $[A]$ has four columns; the first three columns represent the 27 combinations of the independent variables (WFR , TS , and n) based on the DOE, and the fourth unit column represents a constant value added to the model equation. Matrix $[B]$ contains the values of w or h , respectively, for each regression model. A more advanced approach considering a minimization of the mean square error, such as the Levenberg-Marquardt method, could also be used for modeling.³² Alternatively, principal component analysis could be implemented for this purpose. A comparative study of regression approaches and their impact on the model accuracy will be undertaken in future research.

The regression equations obtained via the power law approach were then used to develop a Bayesian network (BN) model. BN modeling is a machine learning method based on Bayes theorem from probability and statistics, which states the likelihood of occurrence based on prior events.³³ BNs have been used in medicine, sports, engineering, and economics to predict occurrence of events by encoding knowledge from historic data, expert opinion, or data collected in real time, or any combination thereof. Heckerman, Geiger, and Chickering³³ identified the key advantages of BN approaches: adept at handling incomplete datasets by encoding statistical dependencies between variables, ability to perform interventions and predict results based on causal relationships, and the ability to combine domain knowledge and data simultaneously to generate sophisticated predictive models. Panicker et al.³⁴ have previously formulated a methodology to develop a BN based on a causal graph generated using the DACM approach. Mokhtarian et al.³⁵ demonstrated an engineering use case of BNs by developing probabilistic models that predicted the curling defect in metal parts produced using PBF technology. The

fundamental advantage of the BN approach used in this study is the ability to translate the causal graph directly into a BN model and to enable two-way simulation for forward prediction (prognosis) of targets and backward prediction (diagnosis) of input parameters. The simulation of the BN (fig. 4) allows the user to choose values for WFR , TS , and n to obtain the required target values and, simultaneously, allows the user to visualize the effects of inputs on the target values. The backward prediction is useful in manufacturing because the final part dimensions are defined up front by the design requirements. In addition, the BN method provides a validated approach to generate gray box models in which analytic knowledge in the form of equations can be used together with experimental knowledge (data).

Results and Discussion

The experimental process was conducted in two phases. First, an initial set of experiments was carried out for single-bead geometries. The purpose was to fine-tune input parameter values, λ ratio, and fixed parameter values, and to evaluate their relevance for multibead modeling. Second, a full-factorial DOE for a multibead wall design was executed. In this section, the single-bead experimental results are first presented, followed by a discussion of the insights acquired by the authors from the first set of experiments. Lastly, regression modeling performed on the full-factorial DOE as well as Bayesian inference for the multibead model are discussed.

EXPERIMENTAL RESULTS FOR SINGLE-BEAD GEOMETRY

Statistical analysis of the data collected from the single-bead experiments was used to characterize the influence of different WAAM process parameters on print quality. The recorded data were subjected to standard data cleaning. The input parameters and output data (h and w) were normalized, and a two-way analysis of variance (ANOVA) test was conducted to identify the most influential process parameters on the height of the printed bead. The P-test associated with the ANOVA found that five out of the nine initial input parameters were statistically significant in affecting the variation in h (Table 2), namely, WFR , TS , Φ , t_{ign} , T_{end} , and I_{end} .³⁶ The effect of input variables on the mean of h for the single-bead geometry are shown in figure 4.

The influential parameters inferred from this initial study helped validate the high influence of WFR and TS on the weld dimensional quality as identified in the Background section. In addition, the inferences made from the single-bead experiments were used to define a suitable printing strategy for multibead printing. The strategy adopted for the multibead experiments involved printing the layers using a back and forth printing pattern to reduce the height difference across the length of the wall (fig. 3C). The torch was held in a vertical position for the multibead experiment.

The combined effect of Φ and front, back, and side feeding will be evaluated in future studies.

TABLE 2

Two-way ANOVA for single-bead experiments

Source	Degrees of Freedom	Adjusted Sum of Squares	Adjusted Mean Squares	F-Value	P-Value
WFR	3	0.104	0.035	11.270	0.000
TS	3	0.816	0.272	88.560	0.000
α	2	0.346	0.017	5.630	0.004
t_{ign}	3	0.050	0.017	5.410	0.002
I_{ign}	3	0.009	0.003	0.950	0.421
ALC	3	0.182	0.006	1.980	0.121
$SGFR$	3	0.003	0.001	0.290	0.832
T_{end}	3	0.099	0.033	10.800	0.000
I_{end}	3	0.457	0.152	49.620	0.000
Error	133	0.408	0.003
Total	159	2.151

REGRESSION MODEL FOR MULTIBEAD GEOMETRY

Two regression models were developed, one for predicting h and the other for predicting w of the part. Welding parameters WFR , TS , and n were considered as the independent variables. A power law was adopted to relate the independent parameters to the dependent parameters; power laws are suited for representing nonlinear relationships between variables in welding. The regression equations developed for h and w are shown in equations (5) and (6), respectively:

$$h \pm e1 = e^{\alpha 1} \cdot WFR^{\beta 1} \cdot n^{\gamma 1} \cdot TS^{\delta 1} \quad (5)$$

$$w \pm e2 = e^{\alpha 2} \cdot WFR^{\beta 2} \cdot n^{\gamma 2} \cdot TS^{\delta 2} \quad (6)$$

subject to

$$2.5 \leq \lambda \leq 5$$

$$T_w \leq 150^\circ\text{C}$$

where $e1$ and $e2$ represent the tolerances of h and w , respectively (Tables 6 and 7). The equations reinforce the paths connecting WFR , TS , and n to h and w (fig. 2). The equations reinforce the paths connecting WFR , TS , and n to h and w (fig. 2). The importance of WFR and TS was also confirmed from equations (5) and (6). Regression analysis was performed based on the data available from 27 specimens. The regression analyses were performed by converting the power law equation into a linear equation using a natural logarithmic transformation (equation (7)).

$$\ln(h) = \alpha \ln(e) + \beta \ln(WFR) + \gamma \ln(n) + \delta \ln(TS) \quad (7)$$

The following matrices were defined for the regression (equations (8)–(11)):

$$[A] = [(e)(WFR)(n)(TS)]_{27 \times 4} \quad (8)$$

$$[E] \text{ s.t. } [E]^T = [\alpha \quad \beta \quad \gamma \quad \delta] \quad (9)$$

$$[h_{ln}]_{27 \times 1} = [\ln(h)]_{27 \times 1} \quad (10)$$

$$[A_{ln}]_{27 \times 4} = [\ln(A)]_{27 \times 4} \quad (11)$$

where $[A]$ is a matrix of 4 columns and 27 rows, in which e is a unit vector of 2.7183 (Euler's number) and the three other columns contain the combinations of input parameters from the full-factorial DOE (Appendix A); $[E]$ is the output matrix giving the exponents for the factors of the regression equation; and $[h_{ln}]$ is a column vector having 27 rows containing the logarithmic (natural log) numbers of measured values for h that corresponds to the DOE. Similarly, $[A_{ln}]$ is computed by applying natural logarithmic operation to $[A]$. Given these matrices, equation (11) calculates the exponents used in equations (4) and (5) for obtaining power law-based regression equations. In this study, square matrices are used for the regression analysis. However, for a rectangular matrix $[A_{ln}]$, exponents can be calculated using equation (12).

TABLE 3

Values for the exponents of the independent variables

Exponents	For w	For h
α	1.4978	0.0946
β	0.3952	0.3539
γ	-0.0286	0.8608
δ	-0.6730	-0.3583

TABLE 4
Quality metrics for the regression equation

Quality Metric	For w	For h
R^2	0.8562	0.9665
RMSE	0.1056	0.2689

Note: RMSE = root mean square error.

$$[E]_{4 \times 1} = ([A_{lm}]^T \cdot [A_{lm}])^{-1} \cdot [A_{lm}]^T \cdot [h_{lm}] \tag{12}$$

Table 3 represents the coefficients obtained from the regression fit. Thus, the resulting regression equations for w (equation (13)) and h (equation (14)) are as follows:

$$w \pm e2 = e^{1.4978} \cdot WFR^{0.3953} \cdot n^{-0.0286} \cdot TS^{-0.6730} \tag{13}$$

$$h \pm e1 = e^{0.0946} \cdot WFR^{0.3539} \cdot n^{0.8608} \cdot TS^{-0.3583} \tag{14}$$

subject to

$$2.5 \leq \lambda \leq 5$$

$$T_w \leq 150^\circ\text{C}$$

Two quality metrics (i.e., R^2 and root mean square error) were computed for each model with respect to the data from the 27 experiments (**Table 4**).

The equations obtained from the regression analyses were then used to develop a BN using BayesiaLab 8 modeling software.

The modeling and simulation results using BN are discussed in detail in the next subsection.

TABLE 5
Validation results of the Bayesian network model

Exp. No.	Forward Simulation				Predicted Using Regression		Measured Values		Measured Variation		
	WFR (m/min)	TS (mm/s)	n	λ	w (mm)	h (mm)	w (mm)	h (mm)	w (mm)		h (mm)
									Along h	Along L	Along L
1	2.60	11.00	11	3.93	3.70	13.92	3.63	13.86	+0.12	+0.09	+0.15
									-0.13	-0.22	-0.25
2	2.70	11.50	12	3.91	3.73	14.99	3.55	14.72	+0.07	+0.02	+0.12
									-0.07	-0.26	-0.12
3	2.50	10.50	13	3.96	3.69	16.11	3.62	15.54	+0.09	+0.05	+0.12
									-0.07	-0.27	-0.11
4	2.90	12.00	17	4.02	3.85	20.49	3.62	20.41	+0.09	+0.19	+0.11
									-0.09	-0.27	-0.14
	Backward Simulation				Target Values of w and h		Measured Values (CMM)		Measured Variation		
5	2.50	11.00	9	3.78	3.60	11.00	3.49	11.14	+0.10	+0.03	+0.07
									-0.08	-0.22	-0.09
6	2.60	10.00	12	4.33	3.70	14.00	3.80	15.04	+0.05	+0.10	+0.10
									-0.04	-0.12	-0.06
7	2.40	12.00	15	3.33	3.50	18.00	3.39	16.72	+0.07	+0.13	+0.05
									-0.06	-0.17	-0.06

Note: Exp. No. = Experiment Number.

BN MODEL DEVELOPMENT AND VALIDATION

The BN model for the geometrical features (*h* and *w*) for an additively manufactured wall is developed using the regression equations. **Table 5** defines the validation experiments performed to evaluate the error of the regression model to predict targets. Five validation experiments were performed for forward simulation, wherein the users defined the *WFR*, *TS*, and *n* values and the BN model was used to predict the resultant *w* and *h* values. Consequently, three experiments were performed for backward simulation, wherein the user defined *h* and *w* target values and the BN model predicted the values of input parameters to achieve the targets. For the validation experiments, *w*, the variation in *w* along the length, and *h* were measured using a CMM. In addition, the variation of *h* along the length of the wall and the variation of *w* along the *h* of the wall were measured using a profilometer. For measuring the variation in *w* along the length, the walls were divided into four equidistant sections and five measurements per section were taken. The variation of *w* along the length and height of the wall and variation of *h* along the length are shown in **Table 5**. The variation of *h* along the length of the wall is shown in Appendix B. The results of the backward simulation using the BN for the sixth validation experiment is shown in **figure 5**. During backward simulation, the user defined the target *w* and *h* of the part to be printed as 3.6 mm and 11.0 mm, respectively. The Bayesian inference engine was then used to prescribe the values for *WFR* (2.5 mm/min), *TS* (11 mm/s), and *n* (9 layers) to achieve the target width and height. The printed part was then measured using a CMM. The average error for the predicted *w* and *h* were found to be 7.72 and 8.76 %, respectively.

In addition, two quality metrics were computed for the forward and backward simulation, namely, maximum relative error magnitude (MREM) and average relative error magnitude (AREM), to assess the predictability of the model. The metrics are computed as follows (equations (15) and (16)):

$$MREM = \max\left(\frac{|y_i - \hat{y}_i|}{y_i}\right) \quad (y_i \neq 0) \tag{15}$$

FIG. 5 Visualization of the Bayesian inference for backward simulation.

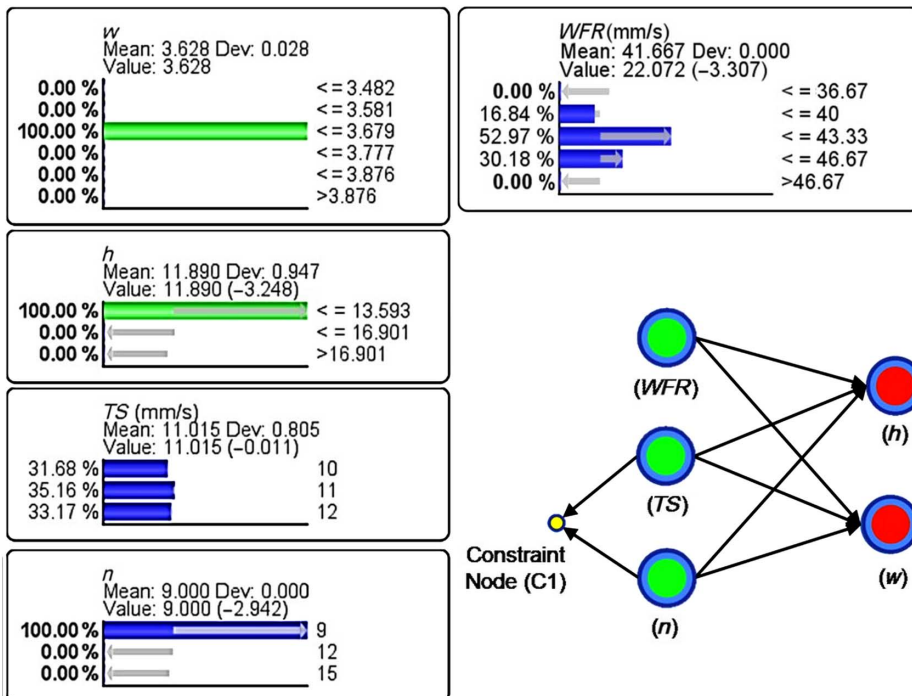


TABLE 6

MREM and AREM values for the regression model

Quality Metric	For w	For h
MREM	2.84 %	3.69 %
AREM	1.83 %	1.44 %
Average ϵ	4.93 %	2.35 %

TABLE 7

MREM and AREM values for the backward Bayesian model

Quality Metric	For w	For h
MREM	4.38 %	3.62 %
AREM	3.03 %	3.09 %
Average ϵ	8.12 %	4.60 %

$$AREM = \frac{1}{m} \left(\frac{\sum_{i=1}^m |y_i - \hat{y}_i|}{y_i} \right) \quad (y_i \neq 0) \quad (16)$$

where y_i is the measured value, \hat{y}_i is the value predicted by the model, and m is the number of data sets. Together, these two metrics evaluate both overall predictability and worst-case predictability of the metamodel.³⁷ Error relative to the variation range of h and w values was also computed as follows (equation (17)):

$$\epsilon = \frac{|y_i - \hat{y}_i|}{\max(y_i) - \min(y_i)} \quad (17)$$

The MREM and AREM metrics for w and h are given in **Tables 6** and **7** for the regression models and Bayesian models, respectively. MREM, which assesses the predictable error in the worst-case scenario, was found to be 2.84 % for w and 3.69 % for h . AREM was found to be 1.83 % for w and 1.44 % for h . Finally, ϵ assesses the accuracy of the model with respect to the range of possible variation of both w and h to characterize the error magnitude better than through relative error computation. The relative error for the developed regression models was found to be slightly higher than that of the best-performing models for width of multibead prints from literature. Sequeira Almeida⁷ predicted the width for multibead prints with relative errors of 0.41, 6.49, and 5.42 % for three experimental validation tests. A relative error of 2.76 % was observed through validation for the model in the worst case.⁷ However, in this work, the error computation follows a more conservative approach to characterize the magnitude of the error. The quality metrics presented in this study show an acceptable accuracy of the model for predicting geometrical dimensions of multilayer parts.

These validation results support the hypothesis that the considered input parameters (WFR , TS , and n) are sufficient to predict geometric dimensions of multibead prints for the CMT WAAM process.

Conclusions

This research presented a graph-based modeling approach combined with regression analysis and BNs to model the width and height of a multibead geometry printed using WAAM. The models for w and h developed in this research are based on three key independent variables associated with the WAAM process (i.e., WFR , TS , and n). The model performance from validation shows a good prediction capability and potential for generalization. The BN implementation enables model expansion to include more variables, such as Φ and filler material type, with verification through future experiments. Because the BN is modular, its scope could be gradually expanded to model other targets. Modularity allows for combining analytical and experimental developments into a single

model. However, to switch between different material systems, additional experiments to determine the optimal value ranges of the two constraints (λ and T_w) are required. In addition, cooling rate has been observed to have a high influence on the final mechanical properties and dimensional quality of the weld. Thus, modeling the cooling rate for different materials will allow for expansion of the BN model to include more targets such as hardness and tensile strength.

Future work will develop causal graphs representing complex phenomena, such as the fluidic and thermal properties of the melt pool, and their impact on final mechanical properties of the printed parts. Characterizing the interrelationships between the thermal properties, initial weld parameters, dimensional quality, mechanical properties, and grain structure of the printed part will enable fast production of high-quality, functional parts on demand using CMT WAAM. More experiments will be conducted wherein the exogenous variables with fixed values in the current research will be converted as independent system inputs to study their influence on WAAM outputs. The model objectives will also be extended to include the effect of using different alloys as filler wire materials. Such expansion would enable development of generic models with extensible scope.

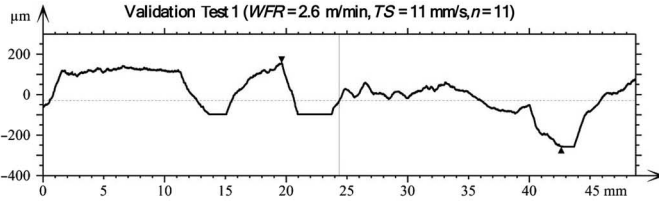
ACKNOWLEDGMENTS

The authors would like to acknowledge Dr. Jari Toiminen of Tampere University for his assistance in defining process settings for this research. The authors would also like to acknowledge Fulbright Finland Foundation for their support of this research.

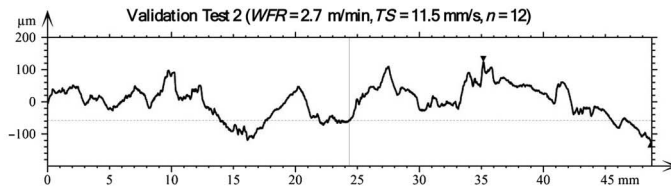
Appendix A: Full-Factorial Design of Experiments for Empirical Modeling of Multibead Geometry in CMT Welding

Experiment	WFR, m/min	TS, mm/s	n	λ Ratio, $1,000WFR/60*TS$	w , mm	h , mm
1	2	10	12	3.333	3.613	14.782
2	2.5	10	12	4.167	4.033	15.327
3	3	10	12	5.000	4.414	16.710
4	2	11	12	3.030	3.268	13.591
5	2.5	11	12	3.788	3.655	14.317
6	3	11	12	4.545	4.013	15.209
7	2	12	12	2.778	3.339	13.150
8	2.5	12	12	3.472	3.512	13.780
9	3	12	12	4.167	3.793	15.303
10	2	10	9	3.333	3.481	11.158
11	2.5	10	9	4.167	3.920	11.683
12	3	10	9	5.000	4.277	12.222
13	2	11	9	3.030	3.367	10.701
14	2.5	11	9	3.788	3.602	11.838
15	3	11	9	4.545	3.695	12.766
16	2	12	9	2.778	3.074	10.542
17	2.5	12	9	3.472	3.363	11.071
18	3	12	9	4.167	3.668	12.064
19	2	10	15	3.333	3.448	17.205
20	2.5	10	15	4.167	3.765	18.228
21	3	10	15	5.000	3.926	19.925
22	2	11	15	3.030	3.274	16.393
23	2.5	11	15	3.788	3.501	18.097
24	3	11	15	4.545	3.806	19.228
25	2	12	15	2.778	3.092	15.839
26	2.5	12	15	3.472	3.387	17.419
27	3	12	15	4.167	3.604	19.443

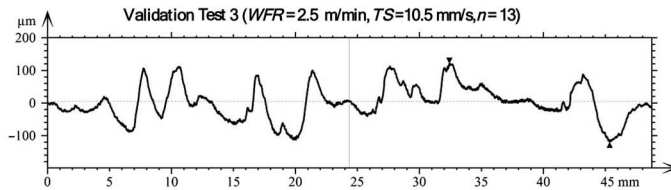
Appendix B: Profilometer Curves for Variation in Height along the Wall



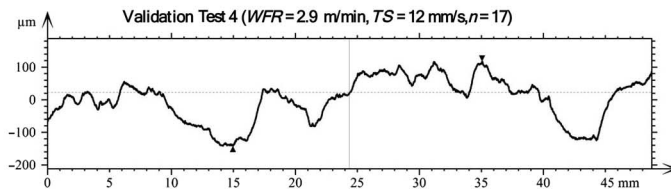
Parameters	Unit	Min Height	Max Height
X	mm	42.6	19.6
Z	μm	-258	155
X (points)	points	42,620	19,631



Parameters	Unit	Min Height	Max Height
X	mm	48.6	35.2
Z	μm	-123	124
X (points)	points	48,647	35,155



Parameters	Unit	Min Height	Max Height
X	mm	45.3	32.4
Z	μm	-119	120
X (points)	points	45,346	32,417



Parameters	Unit	Min Height	Max Height
X	mm	15.0	35.1
Z	μm	-142	118
X (points)	points	14,954	35,053

References

1. S. H. Huang, P. Liu, A. Mokasdar, and L. Hou, "Additive Manufacturing and Its Societal Impact: A Literature Review," *International Journal of Advanced Manufacturing Technology* 67, nos. 5–8 (July 2013): 1191–1203. <https://doi.org/10.1007/s00170-012-4558-5>
2. S. Ford and M. Despeisse, "Additive Manufacturing and Sustainability: An Exploratory Study of the Advantages and Challenges," *Journal of Cleaner Production* 137 (November 2016): 1573–1587. <https://doi.org/10.1016/j.jclepro.2016.04.150>

3. *Standard Terminology for Additive Manufacturing Technologies* (Withdrawn 2015) ASTM F2792-12a (West Conshohocken, PA: ASTM International, approved March 1, 2012). <https://doi.org/10.1520/F2792-12A>
4. D. Ding, Z. Pan, D. Cuiuri, and H. Li, "Wire-Feed Additive Manufacturing of Metal Components: Technologies, Developments and Future Interests," *International Journal of Advanced Manufacturing Technology* 81, nos. 1–4 (October 2015): 465–481. <https://doi.org/10.1007/s00170-015-7077-3>
5. *Standard Guide for Directed Energy Deposition of Metals*, ASTM F3187-16 (West Conshohocken: PA, ASTM International, approved September 1, 2016). <https://doi.org/10.1520/F3187-16>
6. B. Wu, Z. Pan, D. Ding, D. Cuiuri, H. Li, J. Xu, and J. Norrish, "A Review of the Wire Arc Additive Manufacturing of Metals: Properties, Defects and Quality Improvement," *Journal of Manufacturing Processes* 35 (October 2018): 127–139. <https://doi.org/10.1016/j.jmapro.2018.08.001>
7. P. M. Sequeira Almeida, "Process Control and Development in Wire and Arc Additive Manufacturing" (PhD diss., Cranfield University, 2012).
8. Fronius International, "CMT – Cold Metal Transfer: The Cold Welding Process for Premium Quality," Fronius International GMBH, 2019. <http://web.archive.org/web/20190411215014/https://www.fronius.com/en/welding-technology/our-expertise/welding-processes/cmt>
9. C. G. Pickin and K. Young, "Evaluation of Cold Metal Transfer (CMT) Process for Welding Aluminium Alloy," *Science and Technology of Welding and Joining* 11, no. 5 (2006): 583–585. <https://doi.org/10.1179/174329306X120886>
10. E. Välimäki, "Modelling, Simulation and Validation of CMT Process: An Application for Additive Manufacturing" (master's thesis, Tampere University of Technology, 2017).
11. B. Mezrag, F. Deschaux-Beaume, and M. Benachour, "Control of Mass and Heat Transfer for Steel/Aluminium Joining Using Cold Metal Transfer Process," *Science and Technology of Welding and Joining* 20, no. 3 (2015): 189–198. <https://doi.org/10.1179/1362171814Y.0000000271>
12. P. M. Sequeira Almeida and S. Williams, "Innovative Process Model of Ti–6Al–4V Additive Layer Manufacturing Using Cold Metal Transfer (CMT)," in *Proceedings of the 21st Annual International Solid Freeform Fabrication Symposium* (Austin, TX: University of Texas at Austin, 2010), 25–36.
13. J. Näkki, "Properties of Alloy 625 Claddings Made with Laser and CMT Methods" (doctoral thesis, Tampere University of Technology, 2018).
14. N. Pépe, S. Egerland, P. A. Colegrove, D. Yapp, A. Leonhartsberger, and A. Scotti, "Measuring the Process Efficiency of Controlled Gas Metal Arc Welding Processes," *Science and Technology of Welding and Joining* 16, no. 5 (2011): 412–417. <https://doi.org/10.1179/1362171810Y.0000000029>
15. S. Kou, "Heat Flow in Welding," in *Welding Metallurgy* (Hoboken, NJ: John Wiley & Sons, Inc., 2003), 37–64.
16. X. L. Wang, Y. T. Tsai, J. R. Yang, Z. Q. Wang, X. C. Li, C. J. Shang, and R. D. K. Misra, "Effect of Interpass Temperature on the Microstructure and Mechanical Properties of Multi-Pass Weld Metal in a 550-MPa-Grade Offshore Engineering Steel," *Welding in the World* 61, no. 6 (November 2017): 1155–1168. <https://doi.org/10.1007/s40194-017-0498-x>
17. G. Barenblatt, *Similarity, Self-Similarity, and Intermediate Asymptotics* (New York: Consultants Bureau, 1979).
18. S. Ríos, P. A. Colegrove, F. Martina, and S. W. Williams, "Analytical Process Model for Wire + Arc Additive Manufacturing," *Additive Manufacturing* 21 (May 2018): 651–657. <https://doi.org/10.1016/j.addma.2018.04.003>
19. D. Rosenthal, "Mathematical Theory of Heat Distribution during Welding and Cutting," *Welding Journal* 20 (1941): 220–234.
20. N. Nguyen, "Thermal Analysis of Welds," *Applied Mechanics Reviews* 57, no. 6 (November 2004): B34. <https://doi.org/10.1115/1.1849178>
21. Y.-M. Kwak and C. C. Douranidis, "Geometry Regulation of Material Deposition in Near-Net Shape Manufacturing by Thermally Scanned Welding," *Journal of Manufacturing Processes* 4, no. 1 (2002): 28–41. [https://doi.org/10.1016/S1526-6125\(02\)70131-X](https://doi.org/10.1016/S1526-6125(02)70131-X)
22. B. Girinath, N. Siva Shanmugam, and K. Sankaranarayanan, "Weld Bead Graphical Prediction of Cold Metal Transfer Weldment Using ANFIS and MRA Model on Matlab Platform," *Simulation* 95, no. 8 (August 2018): 725–736. <https://doi.org/10.1177/0037549718809162>
23. T. Shao, "Toward a Structured Approach to Simulation-Based Engineering Design under Uncertainty" (PhD diss., University of Massachusetts Amherst, 2007).
24. A. Kroll, "Grey-Box Models: Concepts and Application," in *New Frontiers in Computational Intelligence and Its Applications* (Amsterdam, the Netherlands: IoS Press, 2000), 42–51.
25. E. Coatanéa, R. Roca, H. Mokhtarian, F. Mokammel, and K. Ikkala, "A Conceptual Modeling and Simulation Framework for System Design," *Computing in Science & Engineering* 18, no. 4 (July–August 2016): 42–52. <https://doi.org/10.1109/MCSE.2016.75>
26. R. P. Hanrahan, "The IDEF Process Modeling Methodology," *Journal of Defense Software Engineering* 8 (1995): 1–8.
27. H. Mokhtarian, "Product-Process Integrated Meta-Modeling Using a Graph-Based Approach: Application to Additive Manufacturing" (PhD diss., Tampere University of Technology, 2019).
28. D. C. Montgomery, *Design and Analysis of Experiments* (Hoboken, NJ: John Wiley & Sons, 2017).
29. A. Nabifar, "Bayesian Experimental Design Framework Applied to Complex Polymerization Processes" (PhD diss., University of Waterloo, 2012).
30. Y. Zhang, Y. Chen, P. Li, and A. T. Male, "Weld Deposition-Based Rapid Prototyping: A Preliminary Study," *Journal of Materials Processing Technology* 135, nos. 2–3 (April 2003): 347–357. [https://doi.org/10.1016/S0924-0136\(02\)00867-1](https://doi.org/10.1016/S0924-0136(02)00867-1)

31. M. Linde, *Material Safety Data Sheet (MSDS): Weld G3Si1* (Annapolis Junction, MD: Elektriska Svetsnings-Aktiebolaget, 2012).
32. J. J. Moré, "The Levenberg-Marquardt Algorithm: Implementation and Theory," in *Numerical Analysis* (Berlin, Germany: Springer-Verlag, 1978), 105–116.
33. D. Heckerman, D. Geiger, and D. M. Chickering, "Learning Bayesian Networks: The Combination of Knowledge and Statistical Data," *Machine Learning* 20, no. 3 (September 1995): 197–243.
34. S. Panicker, H. P. N. Nagarajan, H. Mokhtarian, A. Hamed, A. Chakraborti, E. Coatanéa, K. R. Haapala, and K. Koskinen, "Tracing the Interrelationship between Key Performance Indicators and Production Cost Using Bayesian Networks," *Procedia CIRP* 81 (2019): 500–505. <https://doi.org/10.1016/j.procir.2019.03.136>
35. H. Mokhtarian, A. Hamed, H. P. N. Nagarajan, S. Panicker, E. Coatanéa, and K. Haapala, "Probabilistic Modelling of Defects in Additive Manufacturing: A Case Study in Powder Bed Fusion Technology," *Procedia CIRP* 81 (2019): 956–961. <https://doi.org/10.1016/j.procir.2019.03.234>
36. H. Jafarian, "Process Modeling Optimization in Additive Manufacturing Using Artificial Neural Networks" (master's thesis, Tampere University of Technology, 2018).
37. Z. Yang, D. Eddy, S. Krishnamurty, I. Grosse, P. Denno, Y. Lu, and P. Witherall, "Investigating Grey-Box Modeling for Predictive Analytics in Smart Manufacturing," in *Proceedings of the ASME 2017 International Design Engineering Technical Conferences and Computers and Information in Engineering Conference. Volume 2B: 43rd Design Automation Conference* (New York: American Society of Mechanical Engineers, 2017), V02BT03A024.